Proceedings of the ASME 2009 International Mechanical Engineering Congress & Exposition
IMECE2009
November 13-19, Lake Buena Vista, Florida, USA

IMECE2009-10439

AN EFFICIENT NUMERICAL MODEL OF PULSATING COMBUSTION AND ITS EXPERIMENTAL VALIDATION

Luca Casarsa
Dip. di Energetica e Macchine
University of Udine, Italy

Pietro Giannattasio
Dip. di Energetica e Macchine
University of Udine, Italy

Diego Micheli
Dip. di Ingegneria Meccanica
University of Trieste, Italy

ABSTRACT

A simple and efficient numerical model is presented for the simulation of pulse combustors. It is based on the numerical solution of the quasi-1D unsteady flow equations and on phenomenological sub-models of turbulence and combustion. The gas dynamics equations are solved by using the *Flux Difference Splitting* (FDS) technique, a finite-volume upwind numerical scheme, and ENO reconstructions to obtain second-order accurate non-oscillatory solutions. The numerical fluxes computed at the cell interfaces are used to transport also the reacting species, their formation energy and the turbulent kinetic energy. The combustion progress in each cell is evaluated explicitly at the end of each time step according to a second-order overall reaction kinetics. In this way, the computations of gas dynamic evolution and heat release are decoupled, which makes the model particularly simple and efficient. A comprehensive set of measurements has been performed on a small Helmholtz type pulse-jet in order to validate the model. Air and fuel consumptions, wall temperatures, pressure cycles in both combustion chamber and tail-pipe, and instantaneous thrust have been recorded in different operating conditions of the device. The comparison between numerical and experimental results turns out to be satisfactory in all the working conditions of the pulse-jet. In particular, accurate predictions are obtained of the device operating frequency and of shape, amplitude and phase of the pressure waves in both combustion chamber and tail-pipe.

INTRODUCTION

Pulsating combustion is a complex phenomenon that establishes in devices of proper geometry as a consequence of the interaction between an unsteady flow and the heat released by a periodical combustion process.

From the beginning of the twentieth century, pulsating combustion has been used in a wide range of applications such as rocket engines, boilers, hot-air furnaces and dryers [1]. In general, this combustion technique offers advantages like efficient combustion and low emissions of NO_x and CO [2]. Distinctive features of the pulse combustors are the high wall heat transfer, which makes them valuable for thermal applications, and the high thrust/weight ratio when used as jet engines for aeronautic propulsion. Furthermore, pulse combustors are simple, compact and low-cost devices. Of particular interest are the applications in domestic and industrial heating systems (water or air heaters, steam generators, dryers) and in the field of energy production [3]. In gas turbines, the pulse combustor has been proposed as a substitute for the conventional burner or even for the whole compressor/burner unit [1]. Pulsating combustion is considered to have a good potential for development in the field of aerospace propulsion [3]. In particular, the pulse detonation engines, which have been pointed out as the aerospace propulsion systems of the next generation [4], appear to be more efficient than the actual jet engines at both subsonic and supersonic regimes [5] and to represent a better alternative to turbo-fan afterburners [6]. Recently, the use of a pulse combustor has been proposed to obtain a catalyst for the synthesis of nanostructured carbon materials [7].

The renewed interest in pulsating combustion has led to many modeling attempts at different degrees of complexity and detail. Referring to the studies of prevailing interest for thermal applications, which do not consider exclusively the pulsed detonation combustion, the proposed numerical models range

from one-dimensional approaches [8-11] to three-dimensional models using *Large Eddy Simulation* [12][13]. Experimental studies have been also carried out by performing time-resolved measurements of flow field, temperature and heat release inside pulse combustors [14-16].

In spite of the considerably large number of previous studies, some important aspects need to be investigated further on in order to provide efficient and reliable computational tools for pulse combustor design.

In the present work a comparatively simple numerical model is presented for the simulation of pulse combustors, which is claimed to be sufficiently accurate for design purposes. The model is based on a quasi one-dimensional approach to solve the unsteady flow inside the combustor and on phenomenological sub-models of turbulence and combustion. A comprehensive set of measurements, aimed at validating the model, have been performed on a small Helmholtz type pulse combustion engine. Numerical and experimental tests allowed the unsteady behavior of the device to be captured in its whole operating range.

NOMENCLATURE

a speed of sound
A pipe cross-sectional area
c_p specific heat at constant pressure
c_v specific heat at constant volume
d pipe diameter
D_y turbulent diffusion coefficient
e internal energy per unit mass
e_a absolute energy per unit mass
e_f formation energy per unit mass
e^0 total internal energy per unit mass
E mean flow kinetic energy per unit mass
E_a activation energy
f wall friction factor, frequency
f_{st} stoichiometric fuel/air ratio
h enthalpy per unit mass, heat transfer coefficient
h^0 total enthalpy per unit mass
k turbulent kinetic energy per unit mass (TKE)
L length scale of energy-containing eddies
m mass
$\dot{m}$ mass flow rate
M_f fuel molecular weight
Nu Nusselt number
p pressure
P TKE production rate
Pr Prandtl number ($=\mu c_p/\lambda$)
q_w wall heat flux
R gas constant
$\tilde{R}$ universal gas constant
Re Reynolds number
S thrust
t time
T gas temperature
T_w wall temperature
u flow velocity
u' *rms* velocity fluctuation
x space coordinate
y mass fraction

Greek letters

α air/fuel ratio
γ specific heats ratio ($=c_p/c_v$)
ε TKE dissipation rate
λ molecular thermal conductivity
λ_T turbulent thermal conductivity
μ dynamic viscosity
ν kinematic viscosity
ρ density
σ Stefan-Boltzmann constant
ϕ equivalence ratio

Subscripts

a air, ambient
b burnt
cc combustion chamber
e pipe end section
f fuel
g gas
m mixture
st stoichiometric
t partial derivative with respect to time
tp tail-pipe
u unburned
x partial derivative with respect to space

THE PULSE COMBUSTOR

Three main types of pulse combustor can be distinguished: Helmholtz, Schmidt (also known as quarter-wave) and Rijke pulse combustors. They differ in geometry and aero-acoustic behavior, but they all exploit the principle that if combustion heat is periodically added with proper phase to an oscillating gas flow in a pipe, the oscillation is made self-sustaining.

The present work considers a Helmholtz type combustor, a schematic representation of which is provided in Fig. 1. It consists of an automatic valve, an inlet tube, a flame holder, a combustion chamber and a tail-pipe. The device is usually started by using a fan to blow fuel/air mixture into the combustion chamber and a spark plug to ignite the mixture.

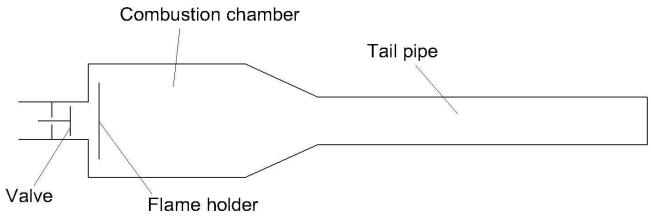

Fig. 1 – Helmholtz type pulse combustor.

Once a stable working condition has been attained, both the fan and the spark plug can be switched off.

The operating cycle of the combustor consists of the following stages:

1) the combustible mixture ignites due to mixing with hot residual combustion products from the previous cycle and to the contact with the hot surfaces of the combustion chamber;
2) the increase in the chamber pressure due to combustion causes the valve to close and the exhaust gas to move outwards through the tail-pipe;
3) burnt gas expands and the pressure in the combustion chamber drops to below the atmospheric value; the chamber empties and the valve opens;
4) the fresh fuel/air mixture enters through the valve as long as the pressure in the combustion chamber is lower than the atmospheric pressure;
5) a compression wave coming from the tail-pipe end causes the valve to close and the charge to be compressed. The fresh fuel/air mixture ignites and the cycle is repeated.

Typically, the cycle frequency of a Helmholtz pulse combustor ranges from 20 to 300 *Hz* [1].

THE MODEL

The present model of the pulse combustor is based on a one-dimensional description of the unsteady flow inside the device and semi-empirical sub-models of combustion and turbulence. In order to reduce the computational cost, the evaluation of the species and turbulence transport and of the combustion progress is decoupled from the computation of the wave propagation inside the combustor.

At each time step, the equations of the quasi-1D unsteady flow of a perfect gas are solved by using a finite volume numerical scheme. The fluxes computed at the cell interfaces are then used to evaluate explicitly the transport of two species (unburned and burnt fuel), turbulent kinetic energy (needed to compute mass and thermal diffusion) and formation energy of the combustion products (needed to compute the heat release). At this point, the solution at the new time is "frozen" and the computation of combustion and heat release is performed at fixed time in each computational cell according to a constant volume process. The combustion sub-model estimates the fraction of burning fuel in the step by means of a second-order overall reaction kinetics. The formation energy of the cell content after combustion is then evaluated by considering the combustion products as formed by six species (CO_2, CO, H_2O, H_2, O_2, N_2) in chemical equilibrium. The heat release in each cell is computed as the difference between the formation energies of the gaseous mixture before and after the combustion step, and the increases in the cell temperature and pressure are consequently evaluated. The solution at the new time level is definitively updated with the values after the combustion and the whole computational procedure is repeated over the next time step. A more detailed description of the various sub-models is provided in the following paragraphs.

Gas dynamic evolution

The quasi-1D unsteady compressible flow in a pipe is described by the vector equation:

$$\mathbf{w}_t + \mathbf{F}(\mathbf{w})_x + \mathbf{S} = 0\,, \tag{1}$$

where the vectors of conserved variables, **w**, fluxes, **F**, and source terms, **S**, have the expressions

$$\mathbf{w} = \begin{Bmatrix} \rho \\ \rho u \\ \rho e^o \end{Bmatrix} \quad \mathbf{F} = \begin{Bmatrix} \rho u \\ p + \rho u^2 \\ \rho u h^o \end{Bmatrix} \quad \mathbf{S} = \begin{Bmatrix} \rho u \sigma \\ \rho u^2 \left(\dfrac{2f}{d} \dfrac{u}{|u|} + \sigma \right) \\ \rho u h^o \sigma - \dfrac{4 q_w}{d} - \dfrac{(\lambda_T A T_x)_x}{A} \end{Bmatrix}$$

and $\sigma = (dA/dx)/A$. Notice that, in order to account for the turbulent diffusion of the combustion heat, the additional term $(\lambda_T A T_x)_x$ has been introduced in the third element of vector **S** compared with the classical formulation of the quasi-1D unsteady flow equations (see, for example, Ref. [17]). System of equations (1) is closed by the perfect gas state equation:

$$p = (\gamma - 1)\rho\left(e^o - u^2/2\right). \tag{2}$$

Equations (1) represent the balances of mass, momentum and energy in conservative form. They reduce to the one-dimensional Euler equations if the vector of the source terms is dropped, i.e., for a frictionless, adiabatic and purely convective flow in a pipe of constant cross-sectional area.

With reference to a computational grid of rectangles $[x_{i-1/2}, x_{i+1/2}] \times [t_n, t_{n+1}]$ in plane (x,t), the integration of eq. (1) leads to

$$\overline{\mathbf{w}}_i^{n+1} = \overline{\mathbf{w}}_i^n - \frac{\Delta t}{\Delta x}\left(\overline{\mathbf{F}}_{i+1/2} - \overline{\mathbf{F}}_{i-1/2}\right) - \Delta t\, \overline{\mathbf{S}}_i\,, \tag{3}$$

where

$$\overline{\mathbf{w}}_i^n = \frac{1}{\Delta x}\int_{x_{i-1/2}}^{x_{i+1/2}} \mathbf{w}(x, t_n)\, dx\,, \quad \overline{\mathbf{F}}_{i+1/2} = \frac{1}{\Delta t}\int_{t_n}^{t_{n+1}} \mathbf{F}\left(x_{i+1/2}, t\right) dt\,,$$

$$\overline{\mathbf{S}}_i = \frac{1}{\Delta x\, \Delta t}\int_{t_n}^{t_{n+1}}\int_{x_{i-1/2}}^{x_{i+1/2}} \mathbf{S}(x,t)\, dx\, dt$$

are the vectors of the average conserved variables in $[x_{i-1/2}, x_{i+1/2}]$ at time t_n, average fluxes in $[t_n, t_{n+1}]$ at cell interface $x_{i+1/2}$ and cell-averaged source terms, respectively. A suitable numerical approximation of the fluxes at interfaces $x_{i\pm1/2}$ and source terms in eq. (3) leads to a finite volume scheme which provides explicitly the solution at new time t_{n+1} in terms of cell-averages of the conserved variables at old time t_n. The numerical fluxes have been evaluated by using the

Flux Difference Splitting (FDS) technique, which is an approximate solver of Riemann problems [18]. Riemann solvers are powerful tools to introduce *upwinding* in conservative schemes for the numerical solution of hyperbolic problems. Upwind schemes take into account the directional propagation of waves that represent the physical basis of the unsteady flow phenomena and, consequently, they propagate the solution in the space-time domain more correctly than the centered methods do. Due to the conservative form of the equations and to the special discretization of the fluxes provided for by the FDS technique, the numerical scheme enjoys the *shock-capturing* property, i.e., it is able to automatically detect and correctly propagate any flow discontinuity (shock waves and contact discontinuities).

The FDS scheme is only first-order accurate in space because the solution at each time is approximated by a series of constant states in the computational cells (piecewise-constant distribution). On the other hand, it is known that higher-order piecewise reconstructions lead to oscillatory solutions if the reconstruction itself is performed according to a linear scheme (Godunov's theorem [19]). In the present work, a second-order accurate solution (in space and time) is obtained by using the *Essentially Non-Oscillatory* (ENO) technique [20]. Thanks to the use of a non-linear reconstruction procedure based on a variable interpolation stencil, this technique allows high-order accurate solutions to be obtained without spurious oscillations.

For the mathematical details of the FDS solver and ENO reconstruction the reader is referred to the literature [18][17].

In the present work, the Euler equations (eqs. (1) with $\mathbf{S} = 0$) are solved at first over the time step by using the FDS-ENO scheme. Then, the source terms are evaluated explicitly halfway through the time step and their contribution is added to the conserved variables to obtain the final solution at new time t_{n+1}. The computational domain is discretized in *N* space intervals and the amplitude of the time step is limited according to the Courant-Friedrichs-Lewy stability criterion:

$$\Delta t = \frac{CFL \cdot \Delta x}{\max\left(|u| + a\right)}, \tag{4}$$

where $CFL \le 1$ is the Courant number. At each time level, term $|u| + a$ is computed in all the space intervals, its maximum value is found and condition (4) is applied to evaluate the next integration time step.

The boundary conditions are computed by using the classical *characteristic boundary* approach [21]. It considers the compatibility equations along the characteristic lines that reach the boundary from the interior of the pipe together with additional conditions mostly based on the assumption of quasi-steady flow. For the computation of the boundary conditions at the pulse combustor inlet the cases of open and closed valve must be distinguished.

In the case of open valve, its steady pressure-flow rate characteristic is usually employed to relate the instantaneous pressure difference across the device to the instantaneous inflow velocity. In the present case, the dynamic response of the automatic (reed) valve cannot be neglected because its first natural frequency (about 195 *Hz*) is very close to the pulse-jet operation frequency and, therefore, a quasi-steady approach is quite inadequate. On the other hand, a sufficiently accurate model of the valve dynamics is difficult to be obtained due to the impact of the reeds on the stop surfaces and to the variation of the contact area between the rear surface of the flame holder and the reeds as they bend, which makes the valve dynamics strongly non-linear. Therefore, it seemed more suitable to perform direct measurements of amplitude and phase of the instantaneous air flow velocity through the intake ports during the pulse-jet operation and to use the corresponding flow rate distribution as a model input. The other boundary conditions in the case of open valve are given by the conservation of the total temperature across the valve and by the compatibility equation along the characteristic line with slope $\lambda^- = u - a$ coming from the pipe interior. When the valve is close, the condition of zero flow velocity is enforced at the inlet section of the combustion chamber and two compatibility equations are written along the characteristic lines with slopes λ^- and $u = 0$.

As the boundary conditions at the tail-pipe open end are concerned, the cases of (subsonic) outflow and reverse flow are distinguished. For the outflow, the pressure at the pipe exit is enforced to be the ambient pressure and the compatibility equations are considered along the characteristic lines with slopes $u > 0$ and $\lambda^+ = u + a$. For the reverse flow from the ambient into the pipe, the momentum equation is written for the inflow through a sharp-edged pipe inlet (Borda nozzle), which leads to condition $p_e = p_a - \rho_e u_e^2$. Moreover, the conservation of the total temperature and the compatibility equation along the outgoing characteristic line, $\lambda^+ = u + a$, are used.

Wall heat transfer

Both forced convection and radiation heat transfer are assumed to contribute to wall heat flux q_w.

The convective heat flux is modeled differently in the combustion chamber and in the tail-pipe. The local heat transfer coefficient in the combustion chamber, which is a region of highly turbulent flow, is computed by means of the Nusselt-Reynolds relationship

$$Nu = a \cdot Re^b, \tag{5}$$

where *a* and *b* are constant. Usual value $b = 0.8$ has been accepted, while constant *a* has been assumed as a tunable parameter of the model. Reynolds number $Re = u_c L/\nu$ is based on the characteristic size of the large-scale eddies, *L*, and local characteristic velocity $u_c = \sqrt{u^2 + u'^2}$, *u'* being the *rms* velocity fluctuation computed from the turbulent kinetic energy ($u' = \sqrt{2k/3}$). The forced convection heat transfer coefficient in the combustion chamber is then computed as

$$h_{cc} = Nu\,\lambda/L\,.$$

The local convective heat transfer coefficient in the tail-pipe is computed as for a fully developed turbulent flow in smooth pipes by means of the Dittus-Boelter correlation:

$$Nu = 0.023\,Re^{0.8}Pr^{1/3}\,. \qquad (6)$$

The Reynolds number is defined as $Re = \rho|u|d/\mu$, where $|u|$ is the absolute value of the instantaneous flow velocity. The heat transfer coefficient in the tail-pipe is then computed as

$$h_{tp} = Nu\,\lambda/d\,.$$

Transport properties μ, c_p and λ of the combustion products are computed as functions of temperature and equivalence ratio as suggested in [22].

The contribution of radiation to the wall heat transfer is evaluated in both combustion chamber and tail-pipe by means of the relation

$$q_{w,rad} = c_R\,\sigma\left(T_w^4 - T^4\right), \qquad (7)$$

where c_R is an adjustable constant.

Finally, the local wall heat flux is computed as

$$q_w(x,t) = h_{cc/tp}(x,t)\left[T_w(x) - T(x,t)\right] + q_{w,rad}(x,t)\,.$$

The wall temperatures have been measured at several stations along the pulse-jet and their piecewise linear interpolation has been used in the model to provide data for $T_w(x)$.

Species and formation energy transport

The gaseous mixture at any location inside the combustor is assumed to be formed of air, fuel vapor and combustion products in chemical equilibrium. To define its composition the following parameters are introduced:

$$y_1 = m_{fu}/m\,, \qquad y_2 = m_{fb}/m,$$

which represent the ratios of the unburned (m_{fu}) and burnt (m_{fb}) fuel masses to the total mass of the gas (m). Furthermore, we define an overall equivalence ratio (ϕ), which refers to the whole fuel mass ($m_f = m_{fu} + m_{fb}$), and a partial equivalence ratio (ϕ_b), which refers to the burnt fuel only:

$$\phi = \frac{m_f/m_a}{\left(m_f/m_a\right)_{st}} = \frac{1}{f_{st}}\frac{m_f}{m_a}, \quad \phi_b = \frac{m_{fb}/m_a}{\left(m_f/m_a\right)_{st}} = \frac{1}{f_{st}}\frac{m_{fb}}{m_a}\,.$$

It is assumed that fuel and air combine always according to the overall equivalence ratio, so that the relation holds $m_{fb}/m_{ab} = f_{st}\phi$, m_{ab} being the combined air mass. Under this assumption parameters y_1 and y_2, or equivalently ϕ and ϕ_b, are sufficient to define univocally the composition of the gaseous mixture.

The following transport equations are written for the uncombined (y_1) and burnt (y_2) fuel:

$$\frac{\partial\left(\rho y_j\right)}{\partial t} + \frac{1}{A}\frac{\partial}{\partial x}\left(\rho u A y_j - \rho D_y A\frac{\partial y_j}{\partial x}\right) = 0\,, \quad j = 1,2\,, \quad (8)$$

where turbulent diffusion coefficient D_y is assumed to be the same for the two species. The discretization of eq. (8) over the *i-th* computational cell leads to

$$\begin{aligned}\left(\rho y\right)_i^{n+1} &= \left(\rho y\right)_i^n \\ &+ \frac{1}{A_i}\frac{\Delta t}{\Delta x}\Big[A_{i-1/2}\left(\rho u\right)_{i-1/2}y_{i-1/2}^n - A_{i+1/2}\left(\rho u\right)_{i+1/2}y_{i+1/2}^n \\ &+ \left(\rho D_y A\right)_{i+1/2}^n\frac{y_{i+1}^n - y_i^n}{\Delta x} - \left(\rho D_y A\right)_{i-1/2}^n\frac{y_i^n - y_{i-1}^n}{\Delta x}\Big] \qquad (9)\end{aligned}$$

where subscript $j = 1,2$ has been omitted for brevity. The mass fluxes at the cell interfaces, $\left(\rho u\right)_{i\pm1/2}$, are known from the solution of eqs. (3), while the values at old time t_n in the cell where the flow comes from are considered for the advected mass fractions $\left(y_1\right)_{i\pm1/2}$ and $\left(y_2\right)_{i\pm1/2}$. The coefficients of the diffusion terms at the cell interfaces are evaluated according to the formula:

$$\frac{1}{\left(\rho D_y A\right)_{i+1/2}} = \frac{1}{2}\left[\frac{1}{\left(\rho D_y A\right)_i} + \frac{1}{\left(\rho D_y A\right)_{i+1}}\right],$$

which is consistent with the equality of the centered and one-side numerical representations of the diffusive fluxes at the cell interface, i.e., it satisfies the conditions

$$\begin{aligned}\left(\rho D_y A\right)_{i+1/2}\frac{y_{i+1} - y_i}{\Delta x} &= \left(\rho D_y A\right)_i\frac{y_{i+1/2} - y_i}{\Delta x/2} \\ &= \left(\rho D_y A\right)_{i+1}\frac{y_{i+1} - y_{i+1/2}}{\Delta x/2}.\end{aligned}$$

In the case of open valve, the boundary conditions for eqs. (8) at the combustor inlet ($x = 0$) are obtained by prescribing the values

$$y_1\big|_{x=0} = f_{st}\phi_{in}/\left(1 + f_{st}\phi_{in}\right), \qquad y_2\big|_{x=0} = 0\,,$$

ϕ_{in} being the equivalence ratio of the entering air/fuel mixture. In the case of close valve, the values of y_1 and y_2 at the boundary are computed by using compatibility equations along the characteristic line with slope $u = 0$. The boundary conditions at the tail-pipe open end are obtained by writing the compatibility equations along the characteristic line with slope $u > 0$ in the case of outflow, while reasonable values of y_1 and

y_2 at the boundary are prescribed in the case of reverse flow from the ambient into the pipe. These values are computed by assuming that the entering flow is a mixture of 50% ambient air and 50% exhaust gas discharged by the device in the previous cycle.

The formation energy per unit mass of the gaseous mixture in each computational cell is evaluated as

$$e_{f,m} = y_1 e_{f,f} + y_g e_{f,g}(T, p_g, \phi) \qquad (10)$$

where $e_{f,f}$ is the constant formation energy of the fuel, $y_g = y_2(1+1/f_{st}\phi) = \phi_b/\phi$ is the mass fraction of the combustion products and $e_{f,g}$ is their formation energy. This latter depends on the equilibrium composition of the burnt gases and, therefore, on mixture temperature *T*, partial pressure of the combustion products p_g and equivalence ratio ϕ. Note that eq. (10) does not include the contribution of the uncombined air because its formation energy is zero by definition. In order to save computational time, the equilibrium compositions of the combustion products (CO_2, CO, H_2O, H_2, O_2, N_2) and the corresponding formation energies are computed once and for all for discrete values of temperature, pressure and equivalence ratio in sufficiently wide intervals ($270 \le T[K] \le 4000$, $0.2 \le p[bar] \le 10$, $0 \le \phi \le 2$). The values of $e_{f,g}$ in the nodes of this three-dimensional domain are stored in a properly formatted input file that is used by the code to compute the gas formation energy for the actual values of *T*, p_g and ϕ by means of 3-D linear interpolations.

Since the absolute internal energy (the sum of formation and sensible energies) of an isolated system is a constant, any change in the formation energy corresponds to an equal and opposite variation of the sensible energy of the system, i.e., to a heat release. In the present work, combustion is modeled as a constant volume process occurring in an isolated system represented by the gaseous content of each computational cell at the end of the time step. Therefore, the heat release due to combustion could be simply computed as the difference between the formation energies of the gaseous mixture before and after the burning process. However, when the combustion products are transported from a cell to another according to eq. (8), their formation energy may change due to temperature and pressure variations and to the mixing with gases of different composition. This contribution to heat release would be completely ignored if the cell value of $e_{f,g}^{n+1}$ before combustion were referred to the equilibrium condition reached in each cell after the transport processes (eqs. (1) and (8)). To overcome this problem the formation energy of the burnt gases before the combustion step has been computed as the result of the transport of $e_{f,g}$ itself, according to the advection-diffusion equation:

$$\frac{\partial(\rho y_g e_{f,g})}{\partial t} + \frac{1}{A}\frac{\partial}{\partial x}\left(\rho u A y_g e_{f,g} - \rho D_y A \frac{\partial y_g}{\partial x} e_{f,g}\right) = 0 . \qquad (11)$$

The discretized form of eq. (11) is similar to eq. (9) and it is not reported for brevity. Also in this case the numerical procedure makes use of the mass fluxes at the cell interfaces computed from eqs. (3) and the transported formation energy is referred to the cell where the corresponding gas flow comes from. The boundary conditions for eq. (11) are obtained by computing the formation energy for the values of T^{n+1}, p_g^{n+1} and ϕ^{n+1} at the end nodes.

Turbulence model

A simple model of generation, transport and dissipation of turbulent kinetic energy (TKE) is used to compute the diffusion coefficients λ_T and D_y in eqs. (1) and (8,11), respectively. Under the hypothesis of isotropic turbulence, the turbulent kinetic energy per unit mass is expressed as $k = \frac{3}{2}u'^2$. TKE is generated by the conversion of the mean flow kinetic energy, $E = u^2/2$, through a kinetic energy cascade process. The kinetic energy contained in large scale turbulent eddies is transferred to smaller and smaller scale structures by an inertial and essentially inviscid mechanism, until molecular diffusion becomes important and viscous dissipation of energy finally takes place. The TKE dissipation rate can be estimated as $\varepsilon \approx u'^3/L$ [23]. The model results in the following transport equation for *k*:

$$\frac{\partial(\rho k)}{\partial t} + \frac{1}{A}\frac{\partial}{\partial x}\left(\rho u A k - \rho D_y A \frac{\partial k}{\partial x}\right) = \rho(P - \varepsilon), \qquad (12)$$

where

$$\varepsilon = \frac{u'^3}{L} = \frac{1}{L}\left(\frac{2}{3}k\right)^{3/2} = 0.5443\,\frac{k^{3/2}}{L}. \qquad (13)$$

The TKE production rate, *P*, is modeled assuming a turbulence production similar to that of a boundary layer over a flat plate [23]:

$$P = \nu_t\, c_E \left(\frac{u}{L}\right)^2, \qquad (14)$$

where $\nu_t = c_\mu k^2/\varepsilon$ is the kinematic turbulent viscosity, $c_\mu = 0.09$ is a universal constant and c_E is an adjustable parameter of the model. If eq. (13) is used to eliminate ε from the expression of μ_t and u^2 is replaced by $2E$ in eq. (14), the TKE production rate takes the form:

$$P = 0.3307\, c_E\, \frac{E}{L}\sqrt{k} . \qquad (15)$$

Two different values are assigned to constant c_E in the combustion chamber (c_{E1}) and in the tail-pipe (c_{E2}) of the pulse combustor, in order to take into account the significantly different geometries and flow conditions. The mean flow kinetic energy *E* in eq. (15) is evaluated on the basis of the instantaneous velocity *u* of the one-dimensional flow, except for the initial portion of the combustion chamber (of length equal to the chamber radius) where *E* is referred, in the case of open valve, to the velocity of the fresh fuel/air mixture emerging from the annular section between the flame holder and the chamber wall.

The discretization of eq. (12) and its numerical solution are performed in the same way as for the transport equations of species. Source terms *P* and ε are evaluated explicitly on the basis of the cell values at old time t_n. As the boundary conditions are concerned, in the case of inflow from the valve or the pipe end the turbulent kinetic energy at the end nodes is estimated as a reasonable fraction of the kinetic energy of the entering mean flow ($k_{in} = 0.1E_{in}$). In the cases of close valve and outflow from the tail-pipe, compatibility equations along the characteristic lines with slope *u* provide the boundary values for *k*.

After evaluating *k* in all the computational cells, the local values of the mass and thermal diffusion coefficients are computed by exploiting the analogy of mass, momentum and energy turbulent transport, which leads to:

$$\alpha_t \approx D_y \approx \nu_t = c_\mu \, k^2 / \varepsilon = 0.1653 \, L\sqrt{k} \,, \qquad (16)$$

where $\alpha_t = \lambda_T / \rho c_p$ is the turbulent thermal diffusivity and dissipation rate ε has been eliminated by using eq. (13).

Combustion rate and heat release

After solving transport equations (1), (8), (11) and (12), the state of the gaseous mixture in each computational cell is completely known at time t_{n+1}, except for the contribution of combustion. The present model assumes an instantaneous heat release at the end of the time step, which results from the change in the formation energy of the cell content due to the burning process. Since the cell properties before and after combustion refer both to time t_{n+1}, they will be distinguished hereafter by indices $*$ and $n+1$, respectively.

According to the model proposed by Longwell e Weiss [24], the combustion rate is expressed by the following second-order overall combustion kinetics:

$$\frac{d\phi_b}{dt} = K\sqrt{T}\,\exp\left(-E_a/\tilde{R}T\right)\frac{f_{st}\rho_a}{M_f}\left(\phi-\phi_b\right)^2 \,, \qquad (17)$$

where rate constant *K* is set equal to $9.5\cdot10^{11}\ \ m^3/K^{1/2}kmol\,s$, as suggested in [24] for hydrocarbon C_8H_{18}, activation energy E_a is assumed as a tunable parameter of the model, and ρ_a is the ratio between the total mass of air (uncombined and burnt) and the cell volume.

Equation (17), the complete derivation of which is shown in [25], is solved at the end of the time step to compute the fuel mass fraction burnt in the step through the corresponding increase in ϕ_b. In each computational cell, eq. (17) is discretized as follows (cell index *i* is omitted for brevity):

$$\phi_b^{n+1} - \phi_b^* = C\sqrt{\overline{T}}\,\exp\left(-E_a/\tilde{R}\overline{T}\right)\rho_a^*\left(\phi-\overline{\phi_b}\right)\Delta t \,, \qquad (18)$$

where $C = K\ f_{st}/M_f$ is a constant, while $\overline{T} = \left(T^* + T^{n+1}\right)/2$ and $\overline{\phi_b} = \left(\phi_b^* + \phi_b^{n+1}\right)/2$ are the mean values of temperature and partial equivalence ratio during the combustion step.

After the burning process, the mass fractions of unburned fuel and combustion products are given by

$$y_1^{n+1} = f_{st}\,\frac{\phi-\phi_b^{n+1}}{1+f_{st}\phi} \,, \qquad y_g^{n+1} = \frac{\phi_b^{n+1}}{\phi} \,, \qquad (19)$$

and the absolute internal energy of the gaseous mixture must be equal to the one before combustion:

$$\begin{aligned} e_{a,m}^{n+1} &= e_{f,m}^{n+1} + c_v T^{n+1} \\ &= y_1^{n+1} e_{f,f} + y_g^{n+1} e_{f,g}\left(T^{n+1}, p_g^{n+1}, \phi\right) + c_v T^{n+1} = e_{a,m}^* \end{aligned} \qquad (20)$$

In eq. (20) the sensible internal energy per unit mass of the mixture is written as $c_v T$, where c_v is assumed to be independent of temperature and composition, consistently with the perfect gas model used in eqs. (1). The partial pressure of the combustion products should be computed as $p_g = \chi_g\, p$, χ_g being the mole fraction of burnt gases. However, the reasonable approximation $\chi_g \cong y_g$ is used, which avoids computing or storing the equilibrium compositions for any set (T, p, ϕ). This approximation is justified by the small number of fuel moles compared to the total one and by the very similar values of the air and burnt gas molecular weights. Furthermore, a small error in the partial pressure of the combustion products results in a much smaller error in their equilibrium composition and formation energy.

Finally, the condition of constant volume process is imposed:

$$p^{n+1} = \frac{p^*}{T^*} T^{n+1} \,. \qquad (21)$$

Relationships (18) through (21) represent a non-linear equation system in the unknowns ϕ_b^{n+1}, T^{n+1}, y_1^{n+1}, y_g^{n+1} and p^{n+1}. Its solution, obtained by means of the Newton-Raphson iterative procedure, allows the final state at time t_{n+1} (after combustion) to be computed in each cell.

EXPERIMENTAL APPARATUS AND PROCEDURE

Figure 2 shows the geometry of the pulse combustor considered in the present work. It is a scale model of a pulse-jet, which exploits the high speed flow of exhaust gas to generate thrust for aeronautic propulsion. The device consists of two main parts: the head, which includes the fuel/air feeding system, and a variable area pipe where the unsteady combustion and flow phenomena take place. The head is configured as an elementary carburetor and it includes a small float chamber, eight air intake ports, a fuel discharge tube, a needle valve for fuel metering and a Venturi nozzle. The fuel/air mixture is fed to the combustion chamber through a reed valve, which consists of ten harmonic steel petals that uncover feed holes as they bend due to the negative pressure in the combustion chamber. The last element of the head is the flame holder, which is shaped as a spherical bowl and acts also as end stop for the reed valve petals. The pipe consists of a single tube of variable cross-sectional area made of stainless steel. The initial portion of larger diameter, which acts as combustion chamber, narrows smoothly to form the tail-pipe, the final portion of which is slightly divergent.

The pulse-jet is started by blowing compressed air through one of the intake ports while generating sparks by means a long piezo-electric igniter inserted manually from the pipe bottom into the combustion chamber. After a self-sustaining combustion has been established, both the delivery pipe of the compressed air and the igniter are removed.

The test rig used to perform the measurements is shown in Fig. 3. The pulse-jet is fixed to the moving part of an aluminum slide. The device head is encased in a duct to allow the measurement of the average air flow rate through the pulse combustor. The duct draws air from the base of a large volume settling chamber, the upper wall of which is connected to a straight pipe that includes a diaphragm for the air flow rate measurement. Two threaded sleeves are welded on the outer walls of combustion chamber and tail-pipe (50 *mm* and 350 *mm* far from the pipe inlet section) to provide seats for a water-cooled piezo-electric pressure transducer (Fig. 3 shows the transducer installed in the tail-pipe). Five temperature taps are mounted on the pipe side at 28, 87, 187, 340 and 500 *mm* from the pipe inlet section. They allow the insertion of Chromel-Alumel thermocouples for the measurement of the inner wall temperature. The pulse combustor is cooled by a high speed air jet coming from a centrifugal fan, the delivery port of which surrounds the combustor head in Fig. 3.

The pulse combustor is fed by a small constant level fuel tank (on the left in Fig. 3) similar to the float chamber of a carburetor. It is supplied with gasoline by a main reservoir not shown in the figure. The measurements of fuel consumption are performed by switching the fuel line from the constant level fuel tank to a measuring burette. This latter is connected to a mechanism that allows the head of fuel to be held constant with respect to the combustor while measuring.

The instantaneous thrust is measured by using an accelerometer and a high-frequency response load cell connected to the slide by means of a double ball joint. Low friction ball bearings are used to minimize the resistance to translation of the slide and the consequent effect on the thrust measurements.

In order to obtain the instantaneous air flow rate to be used as an input data for the model, flow velocity measurements were performed by means of a single-component hot wire anemometer placed just upstream of an intake port of the device head. The simultaneous acquisition of the signals from the hot-wire and the pressure transducer allowed the phase of the intake process with respect to the pressure cycle to be detected.

The experimental data have been acquired by using a general purpose multi-channel acquisition system. The signals from the pressure transducer, load cell, accelerometer and hot-wire have been sampled at the frequency of 20 *kHz*. The data have been post-processed by an in-house developed software, which performs signal filtering and averaging to provide the mean pressure and thrust cycles.

The operating condition of the pulse-jet is univocally determined by the opening degree of the needle valve located in the device head. In fact, the characteristics (amplitude, frequency and phase) of the unsteady combustion and flow

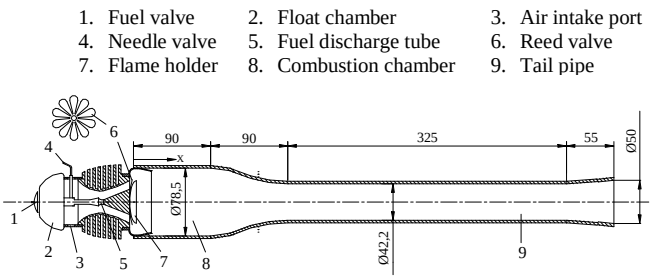

Fig. 2 – Pulse-jet scale model.

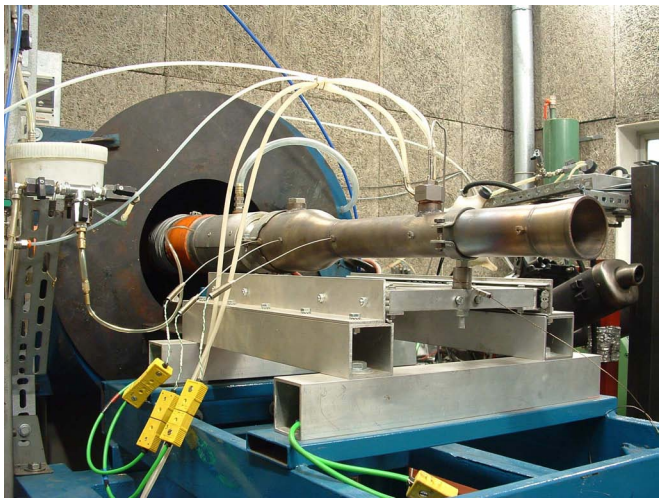

Fig. 3 – Picture of the test rig.

phenomena inside the device depend mainly on the fuel mass introduced and burnt in the combustion chamber per cycle. These unsteady phenomena affect in turn the opening of the reed valve and the mass of fuel/air mixture introduced in the combustion chamber. Therefore, there must be a unique relation between fuel consumption and air mass flow or, equivalently, between fuel flow rate, $\dot{m}_f$, and air/fuel ratio, $\alpha = \dot{m}_a / \dot{m}_f$.

This relation has been found by performing measurements of fuel consumption and average air flow rate for different openings of the needle valve. The measured data are plotted as values of α vs. $\dot{m}_f$ in the diagram of Fig. 4. These data turn out to be well correlated by a linear regression, also reported in Fig. 4 together with the corresponding equation. This correlation has been used in the subsequent experimental tests to identify the operating condition of the pulse-jet, also in terms of air flow rate, on the basis of sole measurements of fuel consumption. Therefore, the connection between the device head and the settling chamber was finally removed, as required by the need of performing thrust measurements.

Finally, the plot in Fig. 4 shows the useful range of air/fuel ratio for a regular combustor operation. It turns out that outside range $11.5 < \alpha < 17$ (the stoichiometric value for gasoline is $\alpha \cong 14.6$) the combustion becomes irregular and tends to extinguish.

Preliminary measurements of pipe wall temperature were also performed to verify that the highest temperature was below the maximum permissible value for the pipe material. The hottest points of the pipe inner wall were detected in the initial portion of the tail-pipe, where temperatures over 600°*C* were measured in spite of the strong cooling effect of the air flow coming from the centrifugal fan. As these temperatures are very close to the limit of material resistance, it was decided to limit the duration of each of the subsequent tests to 2 minutes at most.

RESULTS

In order to obtain correct input data for the numerical simulation of the combustor, measurements of pipe wall temperatures and instantaneous flow velocity through the intake ports of the device head have been performed in several operating condition of the pulse-jet. Subsequently, mean pressure and thrust cycles have been obtained for different air/fuel ratios by processing the signals recorded from the pressure transducer, load cell and accelerometer. Finally, the measured mean cycles have been compared with the computed ones in order to validate the model.

Wall temperature measurements

Figure 5 shows the thermal transient of the pipe inner wall in the five measurement points for $\alpha = 12$ (thermocouples are numbered in increasing order from the pipe inlet section). It can be observed that although steady conditions have not yet reached after the maximum test time (about 120 *s*), the final temperatures differ not much from their asymptotic values. As already mentioned, wall temperatures over 600°*C* are reached at the combustion chamber outlet (tc3) and tail-pipe inlet (tc4), while the maximum temperatures of the combustion chamber wall (tc1 and tc2) turn out to be smaller (from 400 to 500°*C*) also due to the higher effectiveness of the cooling air flow coming from the head side. The coldest wall region is detected near the pipe outlet (tc5), where the influence of the air back flow from the ambient could be important.

Figure 6 shows the dependence of the maximum wall temperatures (after 120 *s*) on the air/fuel ratio. For very rich mixtures, $11.5 < \alpha < 13$, the temperatures turn out to be almost constant, while they decrease smoothly from $\alpha = 13$ up to the flammability limit for lean mixtures, $\alpha \cong 17$. Obviously, this trend is the same as that of the combustion temperatures, which are known to reach their maximum values for slightly rich mixtures.

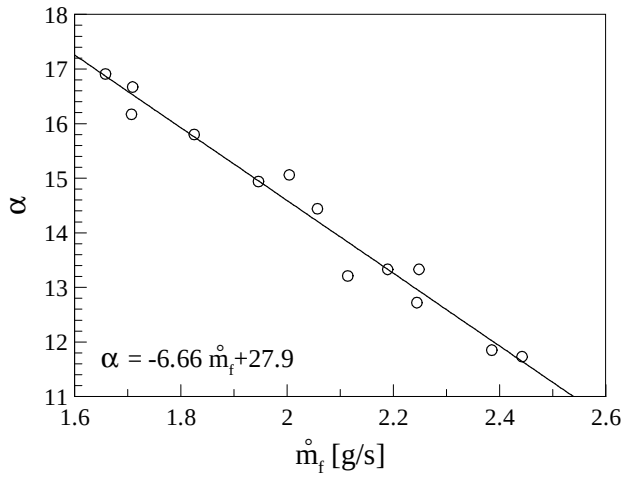

Fig. 4 – Relation between air/fuel ratio and fuel consumption.

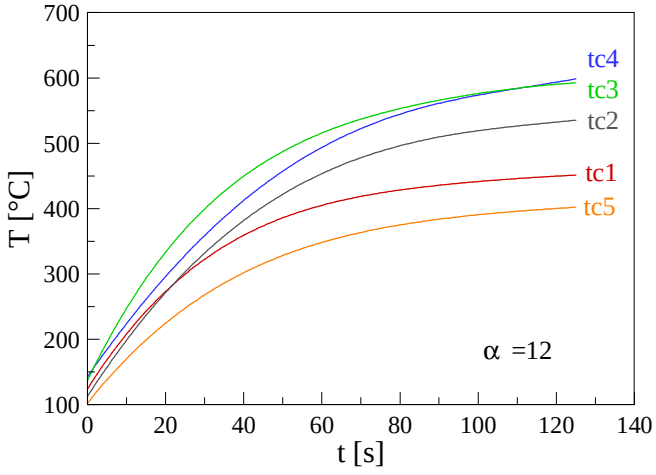

Fig. 5 – Thermal transient of the pipe walls in the five measurement points.

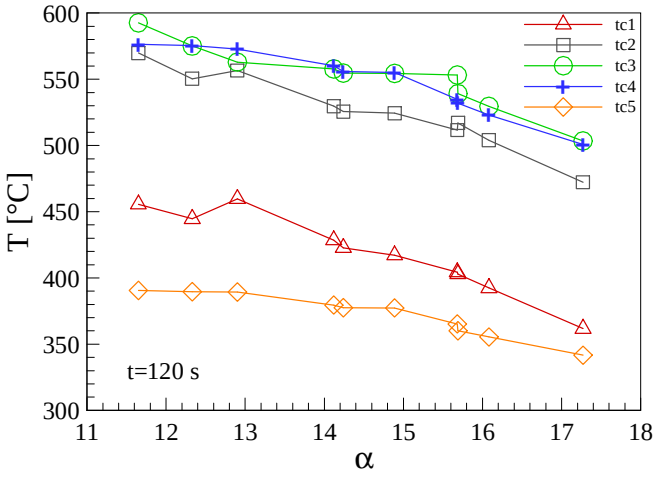

Fig. 6 – Maximum wall temperatures in the five measurement points for different air/fuel ratios.

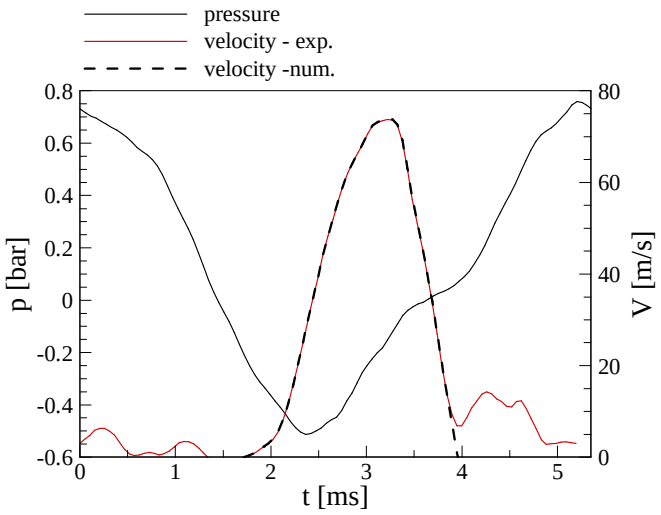

Fig. 7 – Mean cycles of air velocity through an intake port and chamber pressure for α=16.

Measurements of intake air flow velocity

Signals from the hot-wire anemometer and the pressure transducer mounted in the combustion chamber have been acquired simultaneously for one second (corresponding to about 200 operating cycles of the pulse-jet) in several working conditions of the combustor. The data have been post-processed to obtain the mean velocity and pressure cycles, the relative phase of which was determined as the time-lag between the instant when the chamber pressure reaches the atmospheric value and the beginning of the intake period. This time-lag changes slightly around value 0.3 *ms* over the whole variation range of the air/fuel ratio.

As an example, Fig. 7 shows the intake air velocity and chamber pressure mean cycles in the case $\alpha = 16$. The secondary peaks observed in the velocity diagram have been attributed to flow oscillations inside the device head and, therefore, they have not been considered in the intake velocity distribution used as model input (dashed-line curve in Fig. 7).

From air velocity $v(t)$ of a mean cycle, the instantaneous air flow rate entering the device is simply computed as follows:

$$\dot{m}_a(t) = \frac{\overline{\dot{m}_a}}{\bar{v}} v(t) = \alpha\left(\overline{\dot{m}_f}\right) \frac{\overline{\dot{m}_f}}{f \oint v(t) dt} v(t),$$

where $\overline{\dot{m}_a}$ is the average air mass flow rate, $\bar{v}$ is the mean air velocity over the whole cycle, $\overline{\dot{m}_f}$ is the fuel consumption measured during the test, *f* is the cycle frequency and $\alpha\left(\overline{\dot{m}_f}\right)$ is computed from the correlation in Fig. 4. The distribution of the instantaneous mass flow rates of the fuel/air mixture, to be used as a model input, is finally computed as

$$\dot{m}_m(t) = \dot{m}_a(t) + \dot{m}_f(t) = \dot{m}_a(t)\left(1 + 1/\alpha\left(\overline{\dot{m}_f}\right)\right).$$

Pressure cycles in the pipe

Several operating conditions of the pulse combustor have been simulated by means of the proposed numerical model and the computed pressure cycles have been compared with the experimental mean cycles obtained in the middle of the combustion chamber and tail-pipe (50 *mm* and 350 *mm* from the inlet pipe section).

The application of the computational procedure required the preliminary selection of suitable values of the free parameters of the model, namely, the wall friction coefficient, *f*, in eqs. (1), constants *a* and c_R of heat transfer correlations (5) and (7), coefficients c_{E1} (combustion chamber) and c_{E2} (tail-pipe) in eq. (15), and activation energy E_a of the overall combustion kinetics in eq. (17). In spite of the large number of these tunable parameters, the calibration procedure required a moderate effort due to the marked effect of each parameter on specific features of the simulated phenomena. For constants *a* and c_R reasonable variation ranges ($0.035 \le a \le 0.13$, $0.6 \le c_R \le 1.6$) are reported in the literature on internal combustion engines [26][27]. The variations of these parameters result in substantial changes in the average gas temperature and hence in the sound speed. As *a* and c_R are increased the combustion products become colder, the wave propagation in the pipe slows down and the cycle period increases. The separate calibration of these parameters is made easier by the fact that *a* refers only to the combustion chamber, while c_R affects the wall heat transfer in the whole pipe. Constants c_{E1} and c_{E2} influence the TKE production rate and hence the turbulent diffusion of species and heat. In order to mimic the effects of the strongly three-dimensional turbulent flow in the combustion chamber, very high values of c_{E1} are required, at least an order of magnitude larger than c_{E2}. The

main effect of increasing c_{E1} is to promote the simultaneous combustion of larger quantities of fuel, which results in higher peak values of combustion temperature and pressure. The cycle frequency is not sensibly affected by the variations of this parameter. Changes of c_{E2} result in very weak effects as long as its value is kept under few units. Activation energy E_a strongly influences both the combustion intensity and the cycle period. As E_a is increased the ignition delay of the combustible mixture is reduced and more fuel burns in shorter time intervals. Consequently, higher temperatures (and pressures) are reached during combustion and the wave propagation through the hotter burnt gas is sped up, which contributes to shorten the cycle duration. A rather wide variation range for $E_a/\tilde{R}$ (from 16000 to 20000 *K*) is suggested in the literature on engine combustion modeling [28]. Wall friction factor *f* exerts a significant effect on the intensity of the mass oscillations inside the combustor pipe. In practice, its value influences the peak levels of positive and negative pressures generated as the gas in the combustion chamber is compressed by the backflow just before combustion or it expands according to the high speed outflow through the tail-pipe. Preliminary numerical tests showed that very low values of *f* are required in the case of direct flow ($u > 0$), while a friction factor of more than one order of magnitude larger has to be used during backflow ($u < 0$) in order to avoid excessively large overpressures in the combustion chamber. This is consistent with the high friction losses due to the strong separation of the reverse flow at the pipe end section. According to these observations it was decided to introduce two values of the wall friction coefficient, f^+ and f^-, to be used in the cases of direct and reverse flow, respectively.

The tuning of the seven free parameters of the model was performed by comparing the computed and measured pressure cycles in a single operating condition of the pulse combustor, i.e., $\alpha = 16$, and the following optimal values were obtained:

$$a = 0.07,\ c_R = 0.8,\ c_{E1} = 34,\ c_{E2} = 3,$$
$$E_a/\tilde{R} = 17000\ K,\ f^+ = 0.003,\ f^- = 0.05.$$

These values were kept unaltered in the simulation of all the operating conditions of the pulse-jet.

For the properties of the perfect gas mixture, values $\gamma = 1.3$ and $R = 287\ J/kg\,K$ were assumed, which are reasonable for high temperature combustion products. The length scale of the energy-containing eddies was set equal to the clearance between the flame holder and the combustion chamber wall, namely, $L = 13\ mm$.

The combustor pipe was discretized in 200 computational intervals, Courant number $CFL = 0.8$ was used, and the initial conditions for simulation were prescribed assuming that, at $t = 0$, the combustion chamber contains still fuel/air mixture at ambient pressure and 1000 *K* temperature. Starting from this condition, the mixture ignites spontaneously giving rise to an unsteady evolution that results in an exactly periodic oscillation after 10-15 combustor cycles. To allow for a safety margin, 20 complete cycles were simulated in every operating condition of the pulse-jet, which required a computational time of about 5 minutes per run on a modern personal computer.

Figure 8 shows the comparison of computed and measured cycle frequencies for different air/fuel ratios. The agreement between predicted and measured values appears quite good considering the limited frequency range reported in the plot. The decreasing trend of $f(\alpha)$ is explained by the effect of the air/fuel ratio on the combustion temperature and hence on the sound speed in the pipe. As known, the highest flame temperature occurs for slightly rich mixtures ($\alpha \cong 13$) and it decreases as the air/fuel ratio is increased. The wave propagation speed and hence the cycle frequency follow the same path. Anyway, only a moderate variation of the frequency (from 185 to 200 *Hz*) is observed over the whole operating range of the pulse combustor.

Figure 9 reports the predicted and measured mean pressure cycles in the combustion chamber (on the left) and tail-pipe (on the right) in five operating conditions of the pulse-jet. The arbitrary origin, $t = 0$, of the time axis corresponds to the peak pressure in the combustion chamber, and the relative phase of the pressure in the tail-pipe is preserved on the basis of the computed cycles (the availability of a single water-cooled pressure transducer prevented simultaneous measurements in the combustion chamber and tail-pipe to be performed). The pressure in the plots is the relative one, so that $p = 0$ means atmospheric pressure.

The results in Fig. 9 show a satisfactory agreement between numerical and experimental data in the whole operating range of the pulse combustor, since shape, amplitude and phase of the pressure waves in both combustion chamber and tail-pipe appear to be well captured. Only the compression wave preceding the pressure peak in the tail-pipe is systematically underestimated, especially at low values of α.

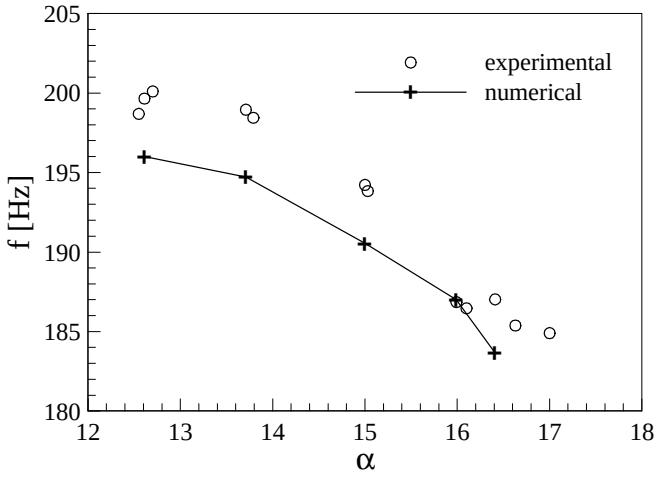

Fig. 8 – Measured and predicted cycle frequencies for different air/fuel ratios.

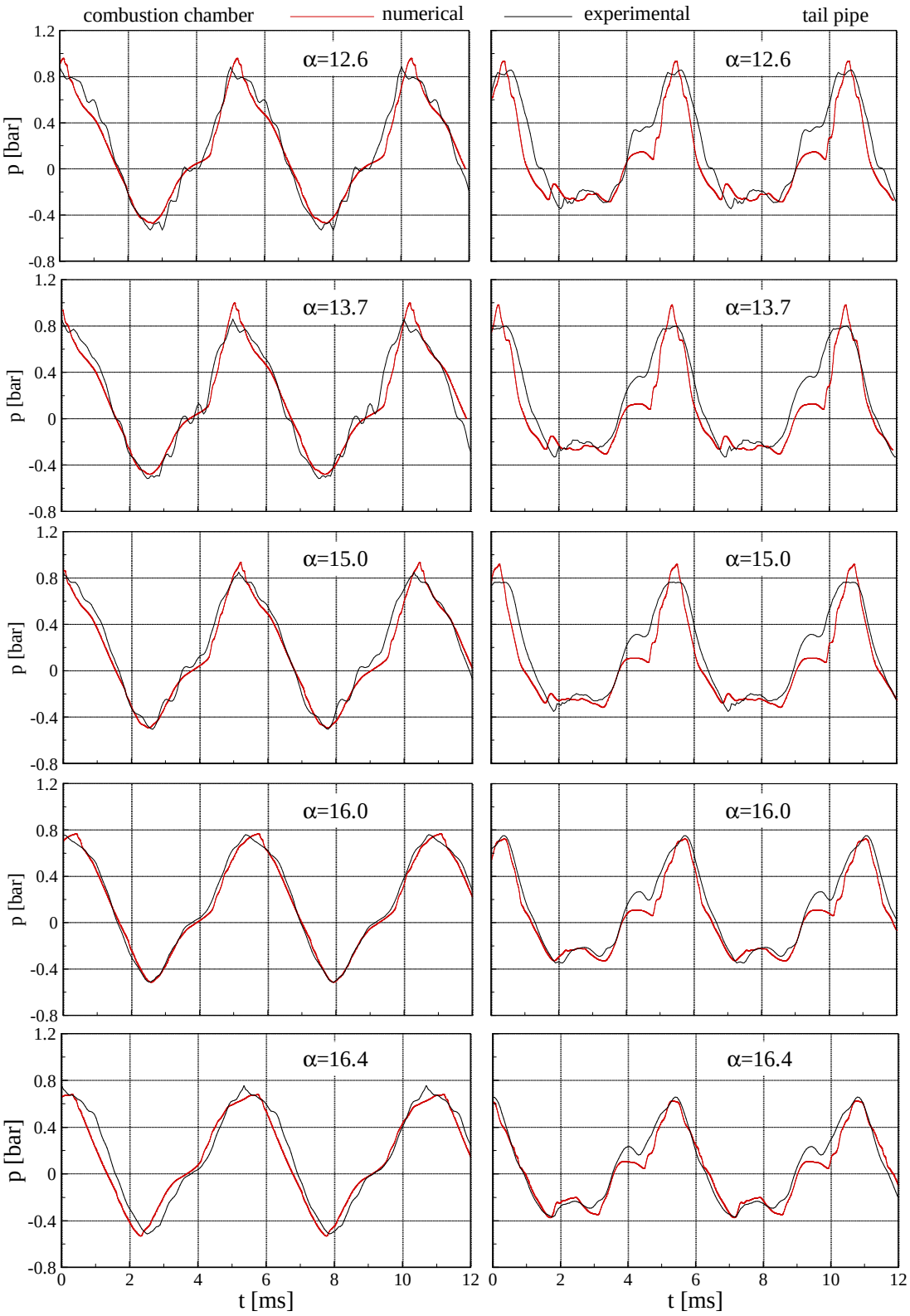

Fig. 9 - Measured and predicted pressure cycles in the combustion chamber (left) and tail-pipe (right) for different air/fuel ratios.

It is observed that as the air/fuel ratio is increased pressure traces become smoother, peak values slightly reduce and, as already discussed, cycle period increases. This behavior is due again to the reduction in the combustion temperature and sound speed at growing α, which result in the slowing down of the wave propagation inside the pipe and a significant attenuation of the high-frequency details.

The numerical results allowed a detailed analysis of the pulse combustor cycle to be performed. Figure 10 shows the computed pressure cycles in the combustion chamber and tail-pipe for $\alpha = 16$. Specific events can be discussed as follows with reference to the 12 time instants marked in the upper side of the plot.

1. Combustion has just finished and the gas temperature is about 1500 *K* everywhere. The burnt gas is still expanding and the flow velocity in the tail-pipe ranges from about 400 *m/s* (at the inlet) to 200 *m/s* (at the exhaust). The reed valve opens about 0.3 *ms* after the chamber pressure has dropped below the atmospheric value. A compression wave, formed at the pipe outlet where the atmospheric pressure is enforced, is going up the tail-pipe.
2. Fresh fuel /air mixture is entering the chamber. The flow velocity has lowered everywhere ($u_{\max} \cong 200\ m/s$ at the tail-pipe inlet). The compression wave from the pipe bottom has just reached the measurement station of the tail-pipe.
3. The fresh mixture front penetrates the chamber. The compression wave has reached the combustion chamber, where pressure begins to go up. A reverse flow ($u < 0$) has just established in the tail-pipe.
4. Due to the backflow through the tail-pipe ($u_{\max} \cong -300\ m/s$) new mass enters the chamber from behind, which contributes to increase the pressure inside it. The gas temperature in the chamber varies rather smoothly from 300 to 1600 *K* as a consequence of the strong turbulent diffusion at the fresh charge/burnt gas interface. In the second half of the tail-pipe the temperature decreases towards the bottom end from 1300 to 600 *K*, due to comparatively cold gas entering the pipe from the outside.
5. The pressure in the combustion chamber has almost recovered the atmospheric value, while the compression wave coming from the chamber has already reached the measurement station of the tail-pipe. The backflow velocity in the tail-pipe has lowered everywhere ($u_{\max} \cong -200$ *m/s* in the diverging end portion of the pipe).
6. Combustion begins in the second half of the chamber, at about 75 *mm* from the pipe inlet section. At the same time the compression wave at the tail-pipe measurement station reaches its maximum amplitude. $u_{tp} \cong$ -100 *m/s* everywhere.
7. Combustion proceeds backward through the chamber and affects increasingly larger portions of fresh fuel/air mixture. High heat release occurs and chamber pressure rises very quickly. Flow velocities are negligible everywhere.
8. The strong compression wave due to combustion has reached the tail-pipe measurement station. Burnt gas begins to accelerate in the tail-pipe.
9. Combustion has moved to the initial portion of the combustion chamber, where gas temperatures as high as 2300 *K* are found. Pressure reaches its maximum values in both combustion chamber and tail-pipe. The time-lag between the pressure waves at the two stations is apparently lost due to the cut-off of the pressure peak in the tail-pipe caused by the flow acceleration in the duct. Flow velocities of about 300 *m/s* are reached at the pipe outlet.
10. A strong expansion of the burnt gas occurs in both chamber and tail-pipe. A maximum flow velocity of about 600 *m/s* is reached in the diverging end portion of the pipe, where a shock wave is formed.
11. Gas expansion continues and high flow velocities (from 300 to 500 *m/s*) establish throughout the tail-pipe. A compression wave resulting from the attenuation of the shock begins to go up the tail-pipe. Most of the fuel/air mixture has been burnt and combustion is coming to its end.
12. The system has come back to the initial condition. The combustion has finished, the reed valve has re-opened and a new intake process is taking place.

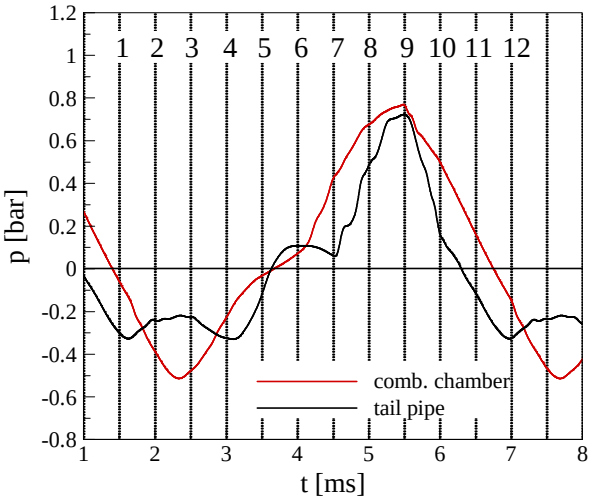

Fig. 10 – Computed pressure cycles for α=16 and reference time instants.

Thrust cycles

The measurement of the instantaneous thrust of a pulse-jet is known to be a difficult task, due to the dynamic response of the mechanical structure to the pulsating excitation force. In order to make this response negligible, so as to use only a load cell for thrust measurements, the slide connected to the pulse-jet was built as light and stiff as possible. In spite of this, measurements showed that the lower natural frequency of the whole system (pulse-jet and slide) was less than twice the excitation frequency, which prevented the dynamic response of the structure to be neglected. Therefore, instantaneous thrust $S(t)$ could only be obtained by performing simultaneous measurements of load cell force $F(t)$ and structure acceleration $\ddot{x}(t)$, according to the dynamic equilibrium equation:

$$S(t) = F(t) - m\,a(t),$$

where $m = 5.15\,kg$ is the mass of the whole system, $a(t) = -\ddot{x}(t)$ is the signal from the accelerometer, and the friction forces between the slide and its guide have been neglected.

The acquired signals turned out to be affected by large amplitude components at frequencies of 1000 *Hz* and higher. These components did not appear to be correlated to the thrust dynamics, being probably associated with the reed valve vibrations or the dynamic response of the slide structure. Therefore, the resulting thrust signals were filtered by using forward and inverse FFT and a cut-off frequency of 900 *Hz*. In this way the fundamental component at about 200 Hz and its harmonics of significant amplitude remained unaltered. Finally, filtered thrust was corrected by adding a constant force of 8 *N* (measured by the load cell with the pulse-jet switched off) due to the contribution of the air flow from the cooling fan.

As the predicted instantaneous thrust is concerned, it is computed from the simulation results according to the momentum equation:

$$S(t) = \frac{\partial}{\partial t}\int_0^{L_p} \rho u\, A\, dx + L_h \frac{\partial \dot{m}_m}{\partial t} + \rho_e u_e^2 A_e + (p_e - p_a)A_e\,. \quad (22)$$

The first and second terms in the right-hand side of eq. (22) represent the time-rate-of-change of the momentum of the gas contained in the pipe (of length L_p) and of the fresh air/fuel mixture in the device head (of length L_h), respectively. The third term is the momentum flux through the pipe end section, while the last term represents the resultant pressure force acting on the pulse-jet outer surface (it is different from zero only in the case of reverse flow). The momentum flux through the intake ports is not included in eq. (22) because the entering flow is nearly perpendicular to the combustor axis.

In Fig. 11 the computed thrust cycles are compared with the measured mean cycles for different operating conditions of the pulse-jet. The agreement between the numerical and experimental results is not so good as for the pressure cycles, the computed traces being much less regular than the measured ones. In particular, a secondary thrust wave, absent in the experimental cycles, is predicted just before the main peak (between about 2.5 and 4 *ms* in Fig. 11). Furthermore, the region of highest thrust exhibits high frequency oscillations that are not observed in the measured mean cycles and the maximum values turn out to be underestimated in all cases.

The secondary thrust wave occurs in the time period of backflow through the tail-pipe (between instants 3 and 6 in Fig. 10). A systematic analysis of the numerical results showed that the momentum flux entering the pipe end section during this period (third term in eq. (22)) is correctly compensated by a decrease in the momentum of the pipe content (first term in eq. (22)), so that no net contribution to the thrust is provided by the reverse flow, as it must be. Also the effects of the second and fourth terms in the right-hand side of eq. (22) were deeply

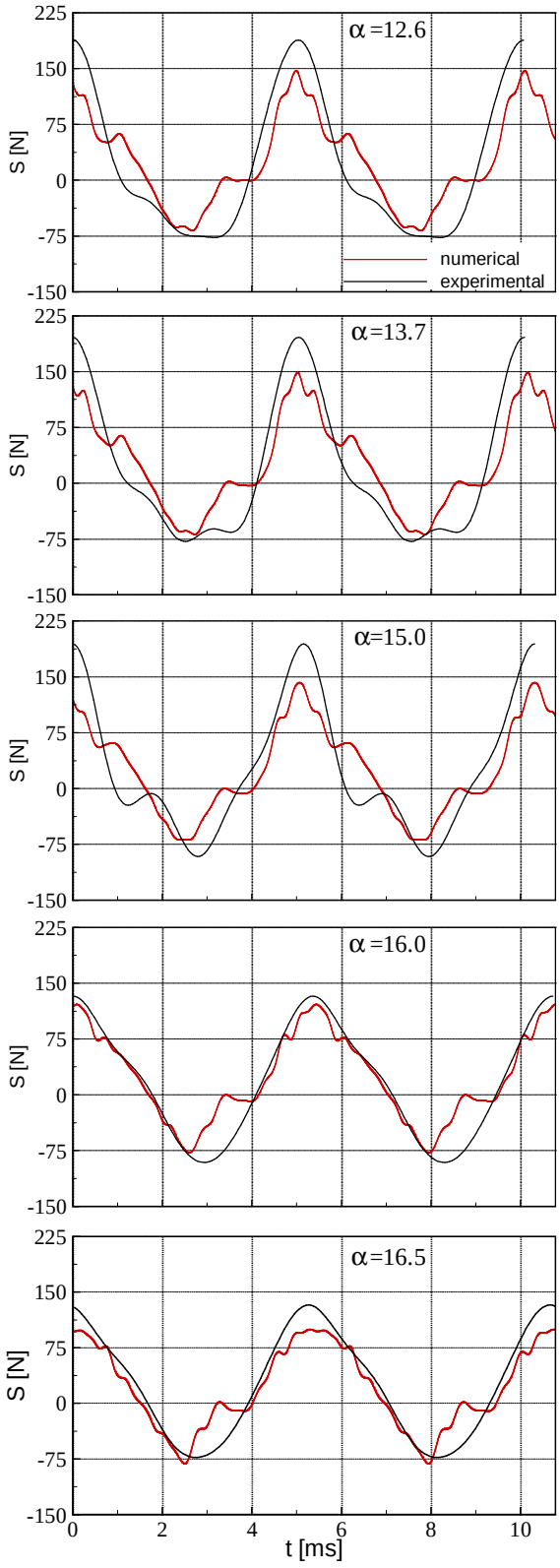

Fig. 11 – Computed and measured thrust cycles for different air/fuel ratios.

investigated, but they could not explain in any way the spurious thrust oscillation. It was concluded that a slightly inaccurate prediction of the pressure and flow oscillations in the pipe during the considered time period could be responsible for the observed behavior. In fact, even small variations in the amplitude and phase of the waves travelling through the pipe were observed to produce significant effects on the time-rate-of-change of the pipe content momentum, which is an integral quantity. On the other hand, also the pressure cycles computed in the tail-pipe (see Fig. 9) showed a systematic underestimation of the amplitude of the pressure wave coming from the combustion chamber at instant 6 in Fig. 10.

The high frequency oscillations predicted in the peak region of the thrust cycle, which corresponds to the combustion period (interval 7-10 in Fig. 10), could be ascribed to an inherent limit of the one-dimensional model. In fact, the simulated combustion proceeds layer-by-layer through the gas contained in the chamber and it can be reasonably expected to be less regular than the bulk combustion occurring in real burners. On the other hand, it cannot be excluded that signal filtering is responsible for the removal of high frequency components due to combustion, if any, from the measured mean cycles. Anyway, the systematic underestimation of the maximum values of the thrust makes the authors inclined to believe that ignoring three-dimensional effects, particularly during combustion, is the main reason for the accuracy limits of the present model.

Finally, Fig. 12 reports the predicted and experimental values of the cycle mean thrust, $\overline{S}$, for different air/fuel ratios. The trend appears to be well reproduced by the numerical model, whereas the predicted values are 10-15% lower than the measured ones. This underestimation is an obvious consequence of the differences between computed and experimental cycles observed in Fig. 11 and commented above.

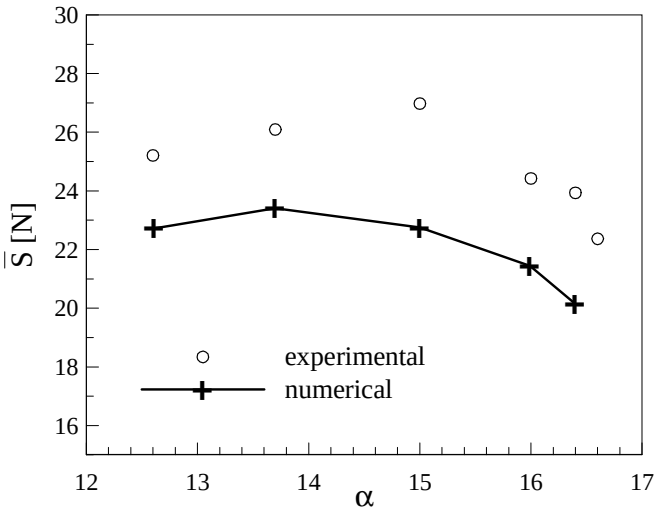

Fig. 12 – Pulse-jet mean thrust in different operating conditions.

CONCLUSIONS

A robust and efficient numerical model has been presented for the simulation of pulse combustors. It is based on a second-order accurate upwind scheme for the numerical solution of the quasi-1D unsteady flow equations and on phenomenological sub-models of turbulence and combustion. The computation of the combustion progress and the transport of reacting species, formation energy and turbulent kinetic energy have been decoupled from the solution of the unsteady flow in the pipe, which makes the model comparatively simple and of low computational cost.

In order to validate the model, time-resolved measurements of pressure and thrust were performed in several operating conditions of a small scale pulse-jet. Sufficiently accurate predictions were obtained of frequency, shape and amplitude of the pressure cycles in both combustion chamber and tail-pipe. Once tuned in a single operating condition of the combustor, the model was able to provide satisfactory results in all the other working conditions, so showing itself to be a robust computational tool for design purposes.

The agreement between predicted and measured thrust cycles turned out to be less satisfactory. This can be partly due to the lower reliability of the thrust measurements compared to the pressure ones, but the authors believe that the main reason is in the inherent limits of a one-dimensional approach, which cannot take into account the effects of the strongly three-dimensional evolution in the combustion chamber. In particular, it is argued that slight differences in the amplitude and phase of the pressure and velocity waves due to 3D effects are not sufficient to produce pressure cycles at fixed locations that are significantly different from the predicted ones. However, they can strongly affect an integral quantity such as the time-rate-of-change of the momentum of the whole pipe content, which results in a scarcely accurate prediction of the instantaneous thrust. In spite of that, the trend of the cycle mean thrust at varying air/fuel ratios was reproduced quite well, which confirms the model capability to capture the essential physics of the pulsating combustion.

Future developments of the present work include the implementation of kinetic models of NO_x and CO formation in the pulse combustor and their experimental validation.

REFERENCES

[1] Putnam, A. A., Belles, F. E., and Kentfield, J. A. C., 1986, "Pulse Combustion", Energy Combustion and Science, **12**, pp. 43-79.

[2] Keller, J. O., Bramlette, T. T., Barr, P. K., and Alvarez, J., 1994, "NO_x and CO Emissions from a Pulse Combustor Operating in a Lean Premixed Mode", Combustion and Flame, **99**, pp. 460-466.

[3] Kezerle, J. A., 1993, "Future Applications of Pulsating Combustion", Workshop in Pulsating Combustion and its Application, Lund, Sweden.

[4] Roy, G., 2001, "Review of Recent Developments in Combustion and Detonation Research", AIAA Paper 2001-0473.

[5] Pegg, R. J., Couch, B. D., and Hunter, L. G., 1998, "Pulsed Detonation Engine Air Induction System Analysis", NASA Langley Research Center and Lockeed Martin Tactical Aircraft Systems.
[6] Mawid, M. A., Park, T. W., Sekar, B., and Arana, C., 2003, "Application of Pulse Detonation Combustion to Turbofan Engines", ASME J. Engineering for Gas Turbines and Power, **125**, pp. 270-283.
[7] Tkachev, A. G., and Baranov, A. A., 2008, "Use of a Pulsating Combustion Apparatus to Obtain a Catalyst for the Synthesis of Nanostructured Carbon Materials", Theoretical Foundations of Chemical Engineering, **42**, 5, pp. 606–610.
[8] Poinzy, B., and Wojcicki, S., 1984, "On Modelling of Pulse Combustors", 20th Int. Symposium on Combustion, The Combustion Institute, pp. 2019-2024.
[9] Morel, T., 1991, "One-Dimensional Fluid Dynamics Model of a Pulse Combustor", Int. Symposium on Pulsating Combustion, C-2, Monterey, California.
[10] Fureby, C., and Lundgren, E., 1991, "One-Dimensional Models for Pulsating Combustion", Int. Symposium on Pulsating Combustion, C-4, Monterey, California.
[11] Barr, P. K., Keller, J. O., and Kezerle, J. A., 1995, "SPDCD: A user-friendly computational tool for the design and refinement of practical pulse combustion system", Int. Gas Research Conference, Cannes, France.
[12] Moller, S. I., Lundgren, E., and Fureby, C., 1996, "Large Eddy Simulation of Unsteady Turbulent Combustion", 26th Int. Symposium on Combustion, The Combustion Institute, pp. 241-248.
[13] Moller, S. I., 1997, "Detailed Numerical Simulation of Pulsating Combustion", Lic. Thesis LRCP 34, Lund Institute of Technology, Lund, Sweden.
[14] Dec, J. E., Keller, J. O., and Hongo, I., 1991, "Time-Resolved Velocities and Turbulence in the Oscillating Flow of a Pulse Combustor Tail Pipe", Combustion and Flame, **83**, pp. 271-292.
[15] Keller, J. O., Barr, P. K., and Gemmen, R. S., 1994, "Premixed Combustion in a Periodic Flow Field: Part 1: Experimental Investigation", Combustion and Flame, **99**, pp. 29-42.
[16] Lindholm, A., 1995, "Time resolved flow fields and heat release in pulse combustors", Lic. Thesis ISSN 0282-1990, Lund Institute of Technology, Lund, Sweden.
[17] Giannattasio, P., and Dadone, A., 1991, "Applications of a high resolution shock-capturing scheme to the unsteady flow computation in engine ducts", Proc. Int. Conf. on Computers in Engine Technology, IMechE, Cambridge, UK, pp. 119-126.
[18] Roe, P. L., 1981, "Approximate Riemann Solvers, Parameter Vectors and Difference Schemes", J. Computational Physics, **43**, pp. 357-372.
[19] Godunov, S. K., 1959, "A finite difference method for the numerical computation of discontinuous solutions of the equations of fluid dynamics", Mat. Sb., **47**, pp. 357-393.
[20] Harten, H., and Osher, S., 1987, "Uniformly High-Order Accurate Nonoscillatory Schemes", SIAM J. Numerical Analysis, **24**, pp. 279-309.
[21] Benson, R. S., 1982, *The Thermodynamics and Gas Dynamics of Internal Combustion Engines*, Volume I, Ed. Horlock J.H. and Winterbone D.E., Oxford University Press, Oxford, UK.
[22] Heywood, J. B., 1988, *Internal Combustion Engine Fundamentals*, McGraw-Hill Inc., New York, NY.
[23] Tennekes, H., and Lumley, J. L., 1972, *A First Course in Turbulence*, MIT Press, Cambridge, Massachusetts.
[24] Longwell, J. P., and Weiss, M. A., 1955, "High Temperature Reaction Rates in Hydrocarbon Combustion", Industrial and Engineering Chemistry, **47**, pp. 1634-1643.
[25] Giannattasio, P., and Micheli, D., 1997, "Phenomenological Modelling of IDI Diesel Engines", SAE Transactions – Journal of Engines, Sec. 3, **106**, pp. 1641-1663.
[26] Annand, J. D., 1963, "Heat Transfer in the Cylinders of Reciprocating Internal Combustion Engines", Proc. I.Mech.E., **177**, 36, pp. 973-990.
[27] Annand, J. D., and Ma, T. H., 1970, "Instantaneous Heat Transfer Rates to the Cylinder Head Surface of a Small Compression-Ignition Engine", Proc. I.Mech.E., **185**, 72, pp. 976-987.
[28] Winterbone, D. E., 1986, *The Thermodynamics and Gas Dynamics of Internal Combustion Engines*, Volume II, Chap. 20 "Transient performance", Ed. Horlock J.H. and Winterbone D.E., Oxford Univ. Press, Oxford, UK.